Sensors and Actuators Reports 8 (2024) 100203

Contents lists available at ScienceDirect

Sensors and Actuators Reports

journal homepage: www.sciencedirect.com/journal/sensors-and-actuators-reports

Fabrication of humidity monitoring sensor using porous silicon nitride structures for alkaline conditions

Soobin Park [a], Inseong Hwang [a], Jae Chan Park [a], Tae Joo Park [a], Han-Seung Lee [b], Sang Yeon Lee [d,e], Hyun-Min Yang [c], Bongyoung Yoo [a,*]

[a] Department of Materials Science and Chemical Engineering, Hanyang University, Ansan 15588, Republic of Korea
[b] Department of Architectural Engineering, Hanyang University, Ansan 15588, Republic of Korea
[c] Department of Sustainable Architectural Convergence Engineering, Hanyang University, Ansan 15588, Republic of Korea
[d] SAT, IMEC, Leuven 3001, Belgium
[e] ESAT, KU Leuven, Leuven 3001, Belgium

ARTICLE INFO

Keywords:
Humidity sensor
Porous silicon nitride
Mace process
Alkaline conditions

ABSTRACT

Porous silicon nitride structures were fabricated for a humidity sensor. The porous silicon structures were fabricated by the metal-assisted chemical etching process, and the conformal silicon nitride thin film was deposited by the atomic layer deposition process. The optimized porous sensor with the 10 nm-thick silicon nitride thin film had a hydrophilic surface and compared to other sensors, had an excellent humidity sensing response. Especially, it showed a superior humidity sensing response at 1 kHz with fast response and recovery times of 13.3 s and 12.4 s, respectively, were observed. Based on the electrochemical impedance spectroscopy results, the equivalent circuits and humidity sensing mechanism were discussed. The chemical stability of the silicon nitride was characterized using Tafel analysis in alkaline electrolytes. Additionally, the sensor's humidity sensing capabilities were tested under cement-embedded conditions.

1. Introduction

Reinforced concrete (RC) structures, which consist of a combination of steel and concrete, are essential in construction fields. Concrete, a mixture of cement, water, sand, and gravel, has high compressive strength. However, because of the poor tensile strength of concrete, steel is used with concrete to enhance the tensile strength. Moreover, due to the small difference in the coefficient of thermal expansion of concrete and steel, there is no internal stress when the temperature changes [1-3]. Additionally, the alkaline conditions of the concrete can protect the steel from corrosion reactions [4-6]. However, as time goes on, the steel in RC structures may no longer be protected from corrosion because corrosive agents can penetrate deep into the concrete.

The corrosive agents that induce steel corrosion in the RC structures directly or indirectly, include chloride ions, carbon dioxide, oxygen, and humidity. Carbon dioxide can decrease the pH of concrete by reacting with calcium hydroxide, which is the primary component of cement along with calcium silicate hydrate [7-9]. The presence of chloride ions can also accelerate steel corrosion [10,11]. Because chloride ions react with iron to make ferrous chloride, a soluble salt, ferrous chloride is dissolved in water in the concrete. After dissolution, ferrous chloride becomes ferrous hydroxide, which is a product of steel corrosion [12, 13]. Humidity, which can operate as the main corrosive agent, provides ion diffusion pathways and creates cracks. During the winter season, when the temperature decreases under 0 °C, humidity can be frozen into ice. Because the volume of ice is approximately 10 % larger than the volume of water, internal stress occurs due to the volume expansion of the water. The induced internal stress can damage the concrete and create cracks. Corrosive agents can penetrate the concrete through these cracks, and the penetrated corrosive agents can cause significant corrosion [14-16]. Furthermore, the steel corrosion and cracks lead to performance degradation of the RC structures, which can cause building collapse [17,18]. To estimate and evaluate the lifetime and durability of RC structures, corrosive agents, especially the humidity, should be monitored.

To detect the humidity, the use of an appropriate humidity sensor is required. A number of studies were conducted to measure the humidity in concrete, and they have employed the passivation using Gore-Tex [19, 20]. In these cases, the humidity sensor electrodes were mounted in plastic tubes with Gore-Tex to protect them from the alkaline conditions

* Corresponding author.
E-mail addresses: yhm04@hanyang.ac.kr (H.-M. Yang), byyoo@hanyang.ac.kr (B. Yoo).

https://doi.org/10.1016/j.snr.2024.100203
Received 31 March 2024; Received in revised form 24 May 2024; Accepted 24 May 2024
Available online 6 June 2024

of concrete. Though the humidity sensor with Gore-Tex can measure the humidity in concrete, a humidity sensor electrode with high chemical stability is needed. If the plastic tubes or Gore-Tex have trouble, it is difficult for the humidity sensor electrodes to measure the humidity accurately in the concrete due to the difficulty of keeping the chemical stability. Therefore, humidity sensing electrodes with high chemical stability itself in alkaline conditions need to be developed to detect and measure the humidity in concrete.

To measure the humidity of concrete, resistive sensors, chilled mirror hygrometers, capacitive sensors, and other commercial systems, such as the HM44 system by Vaisala, which uses the bore-hole method, and the BlueRock system by Giatec, which utilizes the embedded method [21-24]. Those methods were measuring the variation of impedance, resistance, capacitance, and dew point. Azenha et al. reported monitoring and simulating humidity profiles in concrete elements during drying using the HM44 system [23]. They measure the humidity variation by time more than 2 months using the HM44 system. Also, Monazami et.al. reported the performance of carbon fiber-reinforced pavement using BlueRock system sensors [24]. The humidity was measured with embedded conditions and logged from the wireless system. Despite the feasibility of humidity measurement in a concrete embedding environment, the development of humidity sensor electrodes with high chemical resistance is still needed. Because most commercially and widely utilized sensor electrode surfaces were covered with protective materials such as GoreTex. Due to the difficulty of long-term use when damage occurs to the protective materials, the development of electrodes with excellent chemical resistance is challenging.

In this study, we utilized silicon nitride, which has good chemical and mechanical robustness, to fabricate humidity sensing electrodes [25-27]. Silicon nitride was deposited on a porous silicon structure using atomic layer deposition to enable capillary condensation for detecting humidity. Capillary condensation is a natural phenomenon where multilayer adsorption from a vapor into a porous medium proceeds until the pore spaces become filled with condensed liquid from the vapor. In a high-humidity environment, porous media can be filled with water [28, 29]. This approach enables the use of capacitive-type humidity sensors to detect humidity due to the large difference in the dielectric constant of air (almost 1) and water (80) [30-32]. Porous structures are needed for capillary condensation, and we fabricated them using the metal-assisted chemical etching (MACE) process [33,34]. The humidity sensing properties were characterized by analyzing the capacitance variation as a function of the silicon nitride thickness, relative humidity, and frequency. The sensing mechanisms were investigated with electrochemical impedance spectroscopy (EIS). Additionally, the humidity sensing properties of the porous silicon nitride in cement-embedded conditions were investigated.

2. Material and methods

The overall experimental procedure is depicted in Fig. 1. The p-type (100) silicon wafer was used to fabricate the porous structure via the MACE process, using silver nanoparticles as the catalyst. Before experiments, the silicon wafer was cleaved as a coupon wafer with a 1.5 $\times$ 1.5 cm^2 size. The silver nanoparticles were deposited on the silicon surface through a dipping process involving 2 min dip in a 0.02 M tin chloride electrolyte, followed by 30 min dip in a 0.02 M silver nitrate electrolyte. Chemical etching for 6 h in an etching electrolyte comprising 5 M hydrofluoric acid and 4 M hydrogen peroxide led to the formation of the porous surface. The atomic layer deposition (ALD) technique was employed to deposit the silicon nitride, using diisopropylamino silane (DIPAS) as the precursor. First, DIPAS was flowed into the chamber for 1 s, allowing it to attach to the porous silicon surface. Then, using nitrogen gas, a purge process was performed for 15 s. Subsequently, nitrogen (5 N) plasma was used as a reactor (HCP source, 200 W) for 40 s, and another purge process was performed for 20 s. The thickness of the silicon nitride was controlled by varying the number of cycles. Gold/titanium electrodes were deposited on both the top and bottom sides of the fabricated porous Si_3N_4/Si structure using an e-beam evaporator to characterize the humidity sensing properties.

The morphologies and microstructures of the materials were characterized by a field emission scanning electron microscope (FE-SEM, MIRA3, Tescan Co.) and a transmission electron microscope (TEM, JEM-2100F, JEOL). Nyquist plots were measured via EIS with a potentiostat (AMETEK, VersaStat3). Tafel analysis was conducted to confirm the chemical resistivity in a 1 M potassium hydroxide electrolyte similar to concrete conditions.

The humidity sensing experimental setup is illustrated in Fig. 2, which included a mass flow controller, a quartz tube, a commercial hygrometer, a humidity source, and an LCR meter (E4980A, Keysight). The chamber's humidity was controlled by varying the ratio of dry and wet gases generated from the humidity source (Duran SL. BOT2084). The variation of the capacitance was recorded with an LCR meter with AC used to measure capacitance and a voltage of 1 V was applied to the prepared sensor. The humidity changed from 1.6 % to 86.35 %. Before the experiments, the sensor was kept in an oven at 80 °C for several hours to remove any adsorbed water molecules on the sensor surface. The experiment began with the chamber being kept at the lowest humidity, and once the sensing signal stabilized, the humidity was changed by varying the ratio of dry gas to wet gas. The equivalent circuit of the sensor was determined using EIS analysis. EIS was performed using a potentiostat (AMETEK, VersaStat3) to investigate the humidity sensing mechanism. The frequency varies from 1 kHz to 1 MHz with a voltage of 1 V. Tafel analysis was conducted to confirm the chemical resistivity of the fabricated silicon nitride and its promising humidity sensing properties in a 1 M potassium hydroxide electrolyte.

The humidity sensing tests were also carried out with cement paste using ordinary Portland cement with a water-to-cement ratio of 1:2. A mold with a 9 cm diameter and 20 cm height was used to fabricate the specimens. Before being embedded in a cement environment, the porous silicon nitride humidity sensor and a reference humidity sensor (PC Mini 52, Michell) were each covered with a separately fabricated plastic mold with a window-shaped square using 3-D printing. The top and side of the plastic mold were opened. Therefore, the sensor was directly exposed to cement paste. To measure the signals from both sensors, 2-meter-long cables were connected through welding. Subsequently, the fabricated

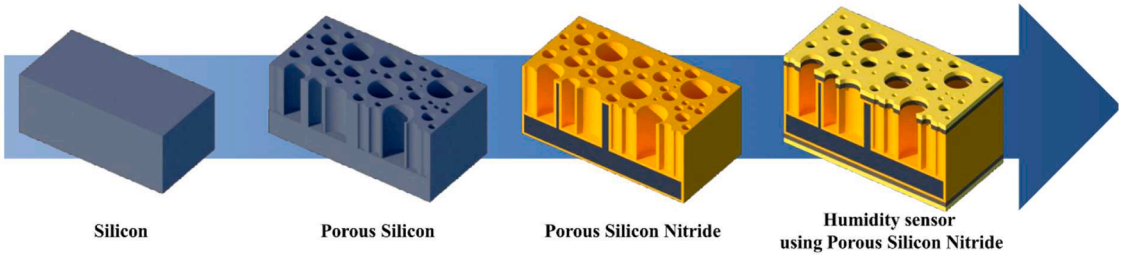

Fig. 1. Schematic illustration of the fabrication process of the porous Si_3N_4/Si structure for the humidity sensor.

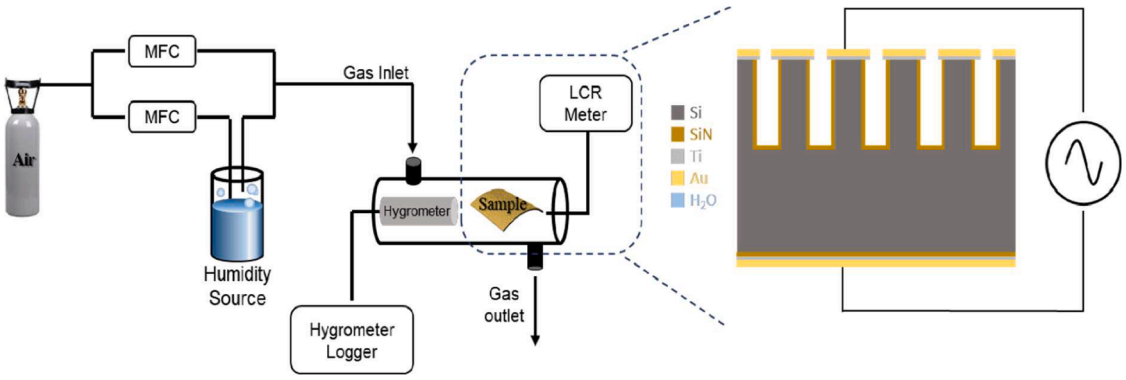

Fig. 2. The schematic illustration of the self-developed experimental environment.

humidity sensor and the reference humidity sensor were positioned at the center of the mold, secured in place with fishing wire, and cement was poured into the mold. After pouring cement into the mold, the samples were kept for 4 weeks for hardening. Following the hardening process, the cement samples were transferred to a chamber.

3. Results and discussion

Fig. 3(a) shows the surface SEM image after the silver deposition process. Silver nanoparticles were deposited onto the silicon surface through the electroless deposition process. The surface SEM images with different electroless deposition conditions are shown in Figure S1 (Supporting Information). When the substrate was immersed in tin deposition electrolytes for 2 min and silver deposition electrolytes for 30 min, uniform silver nanoparticles were distributed on the silicon surface. After the MACE process, the porous structures were formed, as shown in Fig. 3(b). These silver nanoparticles played a role in forming porous structures. As shown in Figure S2 (Supporting Information), the porosity of the silicon surface was increased upon the increased time in the MACE process. Through the silver nanoparticles, catalytic reactions between silicon and hydrofluoric acid occurred to create anisotropic structures [34]. During the deposition process, silicon nitride was deposited onto the porous structure, as shown in Figs. 3(c) and (d). The silicon nitride thin film was characterized as Si_3N_4 by using TEM-EDS (energy

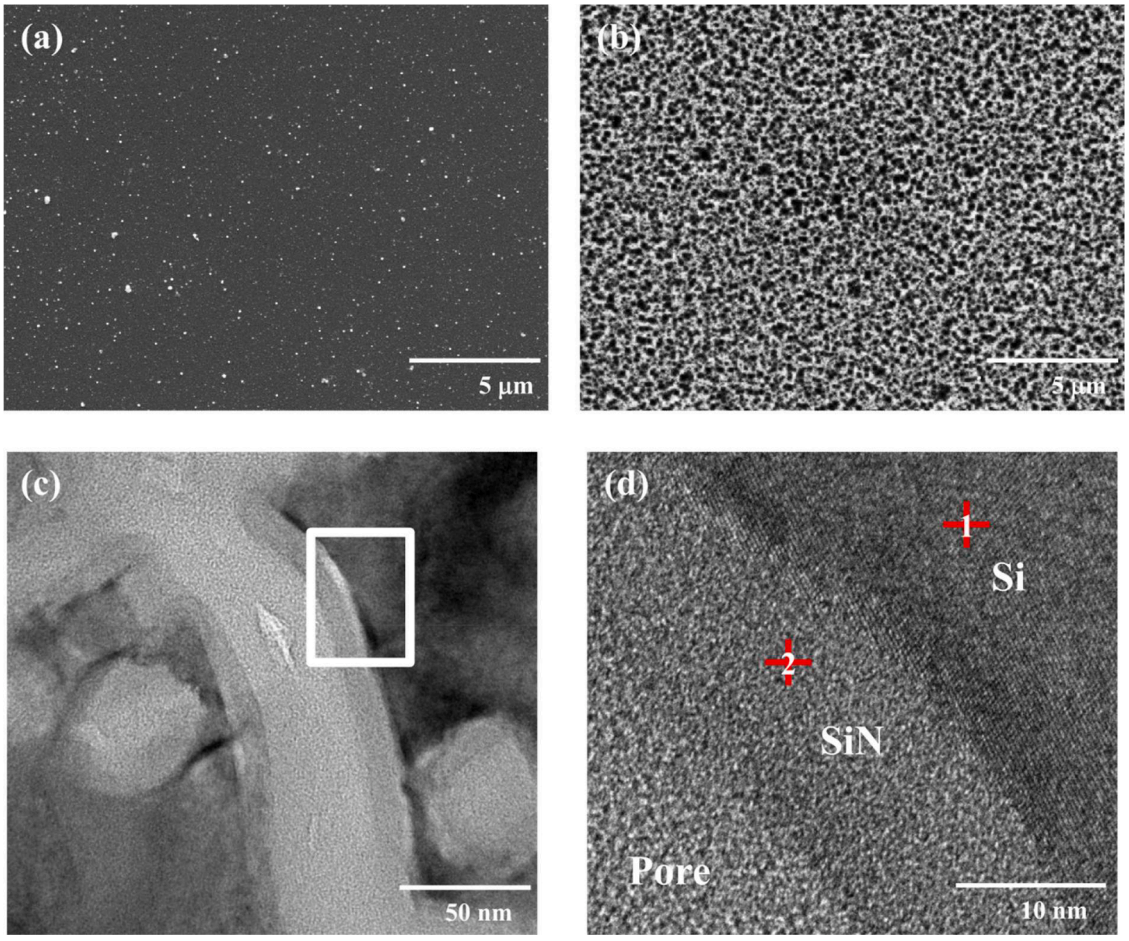

Fig. 3. (a) The surface SEM image after silver deposition on silicon, (b) the surface SEM image after the MACE process, (c) the vertical TEM image after silicon nitride deposition process, and (d) the high-resolution TEM image after silicon nitride deposition process.

dispersive spectroscopy) and XPS (X-ray photoelectron spectroscopy) [35], as shown in Figure S3 (Supporting Information). From Figure S3 (a), there were bare Si, Si-N, and Si-O peaks were deconvoluted at 99.6 eV, 101.4 eV, and 102.6 eV, respectively. From Figure S3 (b), N-Si and N-Si-O peaks were deconvoluted at 397.1 eV and 398.7 eV, respectively. There is oxygen in the silicon nitride film, however, after silicon nitride deposition, the film was exposed to air condition to perform the XPS analysis. Therefore, native oxynitride can be formed on the surface, and it was detected by XPS analysis. The ALD process was utilized to deposit the silicon nitride on the porous silicon, resulting in excellent coverage, as revealed through TEM analysis.

The results of the contact angle test with different silicon nitride thicknesses are presented in Fig. 4. The bare silicon wafer, which included native silicon oxide, had a contact angle of 48.5°. Hydrophobic characteristics were revealed after the MACE process, increasing the contact angle to 137.6° due to the porous surface [36,37]. However, as the silicon nitride thin film was deposited, the surface was changed from hydrophobic to hydrophilic. The 10 nm thick silicon nitride showed a contact angle of 15.3°, which increased to 31° with 30 nm thick silicon nitride. Despite the stoichiometry of Si_3N_4 in the silicon nitride thin film as determined by XPS analysis, which is known to have hydrophobic characteristics, the fabricated porous silicon nitride structure was found to be hydrophilic.

For humidity sensing experiments, the humidity varied from 18.48 RH % to 81.67 RH %. The humidity sensing characteristics of porous silicon nitride are plotted in Fig. 5. The humidity sensing response with different silicon nitride thicknesses at a frequency of 1 kHz is shown in Fig. 5(a). At a thickness of 10 nm, the highest capacitance was observed, and the highest capacitance variation was also observed during the humidity variation. The humidity sensor with 5 nm thick silicon nitride was expected to have optimal humidity sensing properties because of its hydrophilicity. However, the humidity sensing properties of this film were not as good as those of the 10 nm thick film; the 5 nm-thick silicon nitride lacked the dielectric properties to act as a capacitor for the humidity sensor. Excluding the 5 nm thick film, the humidity sensing properties revealed a consistent trend with contact angle test results, as exhibited in Fig. 4. Water molecules could easily absorb to the surface when the sensor surface showed high hydrophilicity. Fig. 5(b) shows the impact of frequency on the humidity sensing response for the 10 nm thick silicon nitride. The humidity was changed from 10.78 RH % to 81.64 RH % with 16 steps. At a frequency of 1 kHz, the porous silicon nitride humidity sensor showed the highest capacitance value and variation. As the measuring frequency increased to 10 kHz, 100 kHz, and 1 MHz, the measured capacitance decreased. The relationship between the frequency and capacitance can be described by Eq. (1), where C_0, ε_r, γ, ω, and ε_0 are the capacitance, relative dielectric constant of an ideal capacitor, conductance, angular frequency, and permittivity of free space, respectively [38,39].

$$C = \left(\varepsilon_r - i\frac{\gamma}{\omega\varepsilon_0}\right)C_0 \tag{1}$$

Following Eq. (1), when the frequency increased, the capacitance decreased, and experimental results corresponded well to theoretical expectations except for the 100 Hz condition. Linearity was an important factor in the sensor, and the 10 nm thick film show the superior linearity properties at a frequency of 1 kHz as 0.998, as shown in Fig. 5 (c). The linearity of 0.998 indicates that the humidity sensing characteristics varied linearly with changes in humidity.

Further humidity sensing characteristics of the porous silicon nitride structures are shown in Fig. 6. The single sensing curve of the 10 nm silicon nitride at 1 kHz in 86.35 RH % is shown in Fig. 6(a). The response time and recovery time for humidity sensing, defined as the time to reach 90 % of the total variation, were 13.3 s and 12.4 s, respectively. The reliability of the porous silicon nitride structures for a capacitive

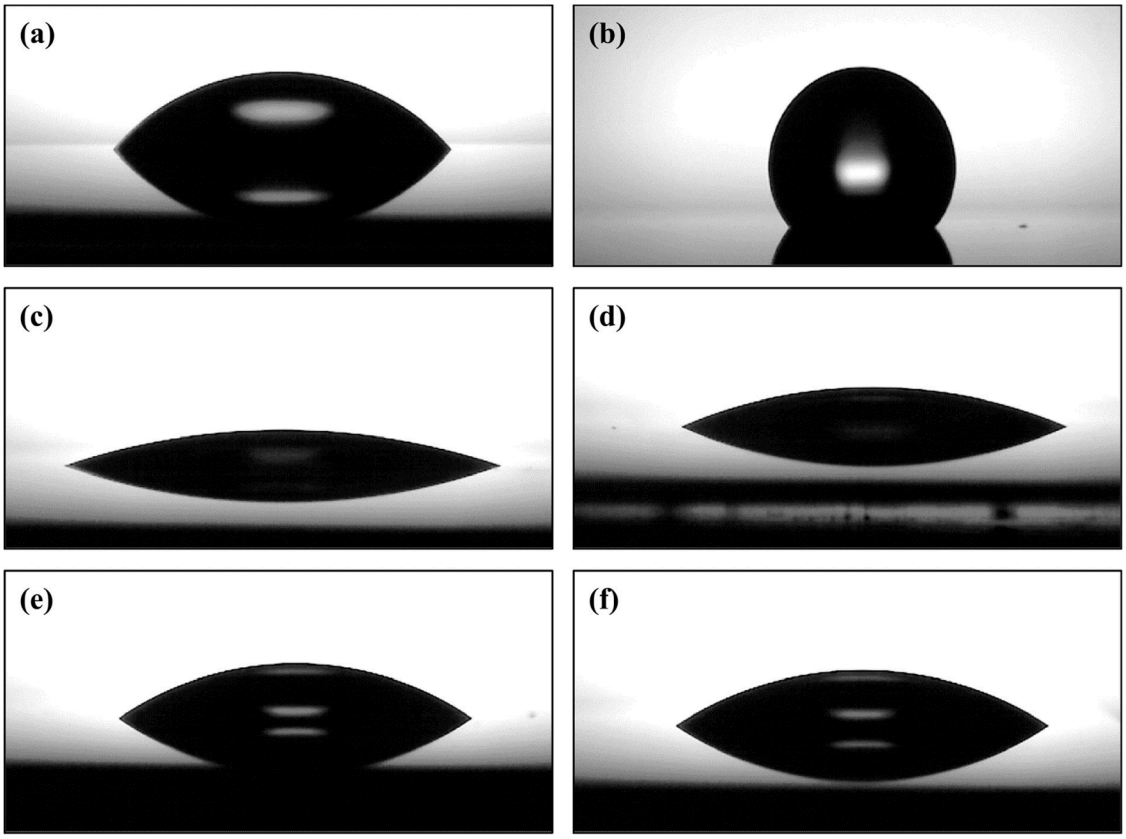

Fig. 4. The results of contact angle measurement with different silicon nitride thickness. (a) The bare silicon, (b) MACE processed porous silicon, (c) 5 nm of silicon nitride, (d) 10 nm of silicon nitride, (e) 20 nm of silicon nitride, and (f) 30 nm of silicon nitride.

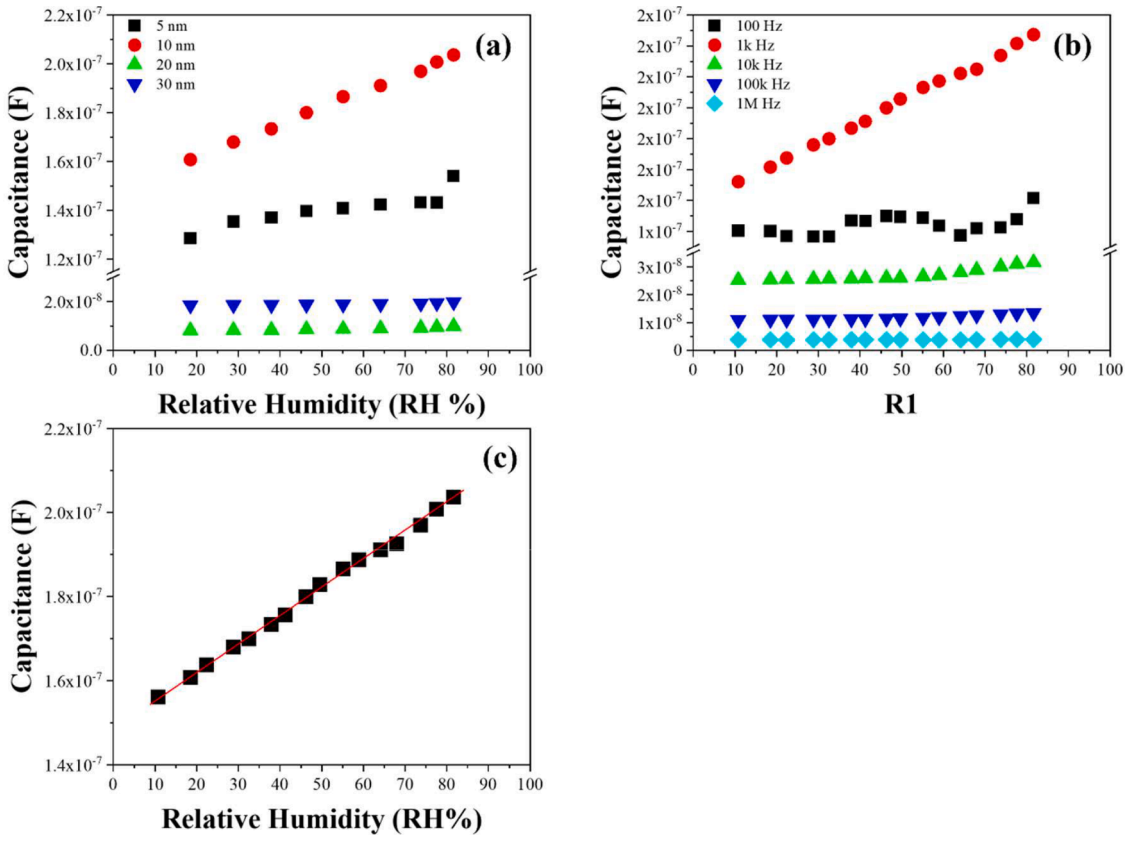

Fig. 5. (a) The humidity sensing properties with different silicon nitride thickness at the frequency of 1 kHz, (b) the humidity sensing properties of 10 nm of silicon nitride with different measuring frequency, (c) the graph of the response with relative humidity variation of 10 nm silicon nitride at the frequency of 1 kHz.

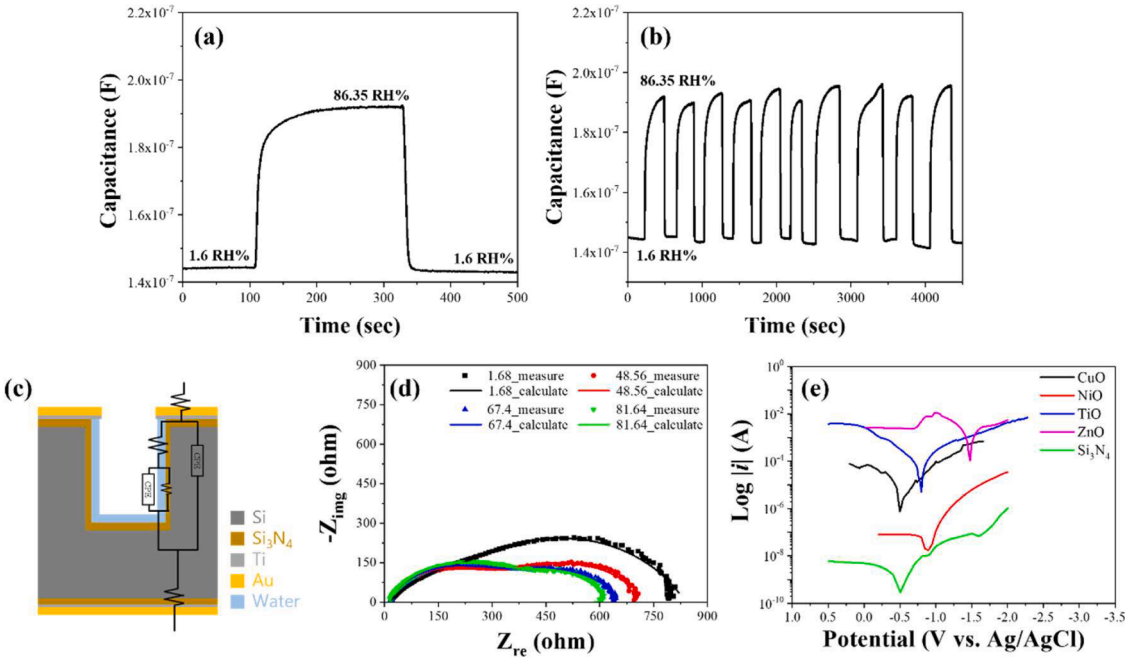

Fig. 6. (a) The graph of single humidity sensing curve at 1 kHz in 86.35 RH %, (b) the repeated humidity sensing test at 1 kHz for 86.35 RH %, (c) the equivalent circuit model and schematic illustration of porous Si_3N_4/Si humidity sensor, and (e) the results of Tafel analysis of CuO, NiO, TiO_2, ZnO, and Si_3N_4 in 1 M of KOH electrolytes.

humidity sensor was also investigated, as plotted in Fig. 6(b). The reproducibility was examined by analyzing the sensing of 10 cycles at a frequency of 1 kHz at 86.35 RH %. When the humidity was changed continuously, the measured capacitance for a specific humidity value was the same. Moreover, long-term stability was characterized in Figure S4. The fabricated sensor electrode demonstrated stable sensing

performance for 40 days at 86.35 RH %.

The humidity sensing behavior of the porous silicon nitride at various humidity levels of 1.68 RH %, 48.56 RH %, 67.40 RH %, and 86.35 RH % was investigated with Nyquist plots using EIS analysis, as shown in Figs. 6(c) and (d). Two semicircles were observed in the complex impedance plots, regardless of the changing humidity levels. The semicircles represent the behavior of the intrinsic impedance of the porous silicon nitride structure and the pores, indicating an equivalent circuit of $R(Q_{Si}(R(Q_{pore}R)))$. This is described in Fig. 6(c), which shows the vertical graphical illustration of the porous silicon nitride structures and electrochemical equivalent circuits. In the equivalent circuit of the humidity sensor structure using Q, the constant phase element (CPE) was used instead of the capacitance (C) because of its porous surface morphology. The capacitance should be replaced with CPE if the electrode surface has a porous structure [40,41]. The initial Q was represented as Q_{Si}, which is the CPE factor of the silicon substrate. And the following Q was represented as Q_{pore}, which is the CPE factor of silicon nitride. The silicon nitride was deposited on the porous silicon structure, therefore, it can be replaced with CPE because of its rough surface. As the humidity increased, the resistance, R_{ct}, of the porous silicon nitride structure decreased, displaying a decrease in the radius of the overall Nyquist plots. Moreover, with increasing humidity levels, the capacitance, C_{water}, gradually increased, displaying an increase in the radius of the first semicircle in the Nyquist plots. In dry conditions, porous media filled with air have a low dielectric constant. However, as the humidity increased, water molecules were adsorbed in the porous parts of the porous silicon nitride structure. Through capillary condensation, adsorbed water layers were formed in the porous media; these had a high dielectric constant [30-32]. The transition of the dielectric constant affected the total capacitance, as described by Eq. (1), and the increased dielectric constant induced an increase in the capacitance. Therefore, with an increase in the humidity levels, the measured capacitance of the porous silicon nitride humidity sensor was changed due to the higher dielectric constant of water.

Fig. 6(e) shows the Tafel analysis results of the fabricated humidity sensor electrodes with porous silicon nitride structures and promising humidity sensing materials, which were zinc oxide, cupric oxide, nickel oxide, and titanium oxide. The Tafel analysis was conducted in 1 M potassium hydroxide electrolytes, imitating alkaline concrete conditions. The silicon nitride thin film was characterized to have a corrosion potential of −437.23 mV and a corrosion current of 765.70 pA. However, the cupric oxide, zinc oxide, nickel oxide, and titanium oxide were characterized to have corrosion potentials of −522.73 mV, −1475 mV, −831.72 mV, and −785.445 mV, respectively. Additionally, the corrosion currents for these materials were determined to be 5.24 μA, 7.97 mA, 103.51 nA, and 183.08 μA, respectively. In the Tafel analysis, the thin film had excellent corrosion characteristics when it was characterized to have a positive corrosion potential and a small corrosion current [42,43]. Silicon nitride was revealed to have the best chemical resistivity in alkaline conditions due to its most positive corrosion potential and smallest corrosion current. Through Tafel analysis, it was determined that the porous silicon nitride structure can be successfully utilized in a cement-embedded humidity sensor.

Fig. 7 shows the results of the cement embedding experiments using the porous silicon nitride humidity sensor. Before starting the humidity monitoring with concrete-imitated environments, the sensor-embedded specimen was moved into a chamber for drying. After the specimen moved into the chamber, the humidity monitoring was started. In the initial condition, the humidity of the specimen was observed at 91.8 RH %. After 100 h, the specimen gradually dried in the chamber to 41.7 RH %. Upon the change of humidity, variations in the capacitance of the porous silicon nitride humidity sensor were logged. As the humidity decreased, the capacitance of the embedded humidity sensor also decreased. After the drying period, the cement specimen was immersed in a beaker filled with tap water for humidifying. At the initial state of humidifying, the humidity of the specimen was not changed because it required time for diffusion of the humidity inside to reach the humidity sensor. The humidity of the cement specimen was increased to 91.8 RH % after 50 h of humidifying. The embedded porous silicon nitride humidity sensor detected humidity variations in the cement. Fig. 7(b) shows the graph of the capacitance with humidity. The capacitance decreased during the drying period, but it showed exponential behavior. The capacitance was increased linearly during the humidifying experiments, and the linearity was fitted as 0.989 based on the Pearson correlation coefficient r.

4. Conclusion

In conclusion, the porous silicon nitride structures were fabricated and optimized for humidity sensors. The MACE process was conducted to form porous structures using silver nanoparticles as catalysts. Silicon nitride was deposited via the ALD process at thicknesses of 5, 10, 20, and 30 nm to form the sensing materials. From the results of the contact angle testing, the silicon nitride showed hydrophilic characteristics, and as the thickness of silicon nitride increased, the hydrophilicity decreased. The 10 nm thick deposited sensor showed a superior sensing response. Moreover, it showed linear sensing behavior and the highest response value at a frequency of 1 kHz. The response time and recovery time for the 81.64 RH % conditions were 13.3 s and 12.4 s, respectively. From the EIS results, the equivalent circuit of the humidity sensor was fitted as $R(Q_{Si}(R(Q_{pore}R)))$. Because of the porous surface, CPE was better matched than capacitance. Additionally, two semicircles were clearly revealed in the Nyquist plots. Based on the Tafel analysis, silicon nitride had excellent chemical resistivity in alkaline conditions, as

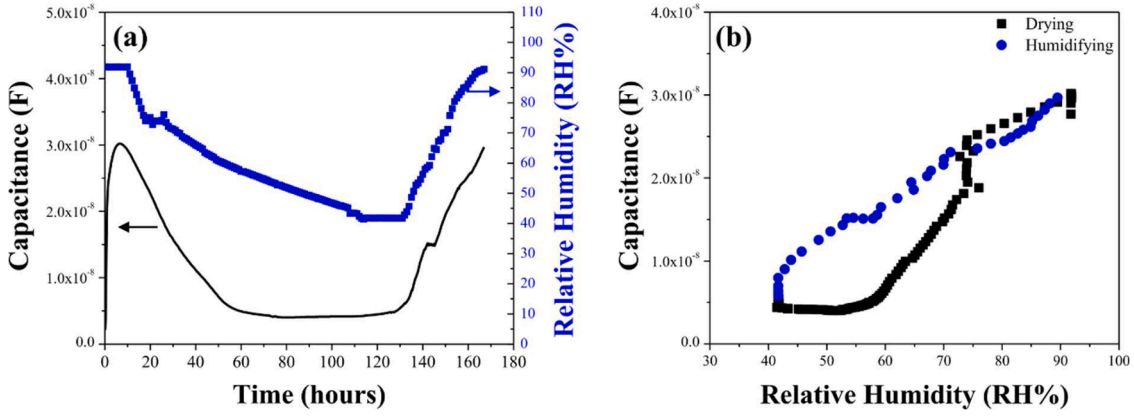

Fig. 7. The results of the humidity sensing properties of porous Si_3N_4/Si structure in cement embedded conditions. (a) The variation of the capacitance of porous Si_3N_4/Si structure with time and (b) the variation of the capacitance with relative humidity in cement.

compared to other humidity sensing materials. In the cement embedding test, the porous silicon nitride humidity sensor detected humidity variations in the cement. Moreover, it showed linear humidity sensing behavior during the humidifying process. From the humidity sensing experimental results, we show that a humidity sensor with a porous silicon nitride structure has the potential to detect and measure the humidity of cement under embedded conditions.

CRediT authorship contribution statement

Soobin Park: Writing – original draft, Validation, Methodology, Formal analysis, Conceptualization. **Inseong Hwang:** Visualization, Investigation, Data curation. **Jae Chan Park:** Investigation, Formal analysis. **Tae Joo Park:** Resources. **Han-Seung Lee:** Supervision, Resources. **Sang Yeon Lee:** Validation, Writing – review & editing. **Hyun-Min Yang:** Writing – review & editing, Supervision, Investigation, Funding acquisition, Conceptualization. **Bongyoung Yoo:** Writing – review & editing, Validation, Supervision, Methodology, Conceptualization.

Declaration of competing interest

The authors declare that they have no known competing financial interests or personal relationships that could have appeared to influence the work reported in this paper.

Data availability

Data will be made available on request.

Acknowledgements

This research was supported by the Basic Science Research Program through the National Research Foundation of Korea (NRF) (No. NRF-2020R1A2C2009462) and MOTIE (Ministry of Trade, Industry, and Energy) in Korea, under the Fostering Global Talents for Innovative Growth Program (P0017312) supervised by the Korea Institute for Advancement of Technology (KIAT). Also, this work was supported by the National Research Foundation of Korea (NRF) grant funded by the Korea government (MSIT) (No. RS-2023-00217322)

Supplementary materials

Supplementary material associated with this article can be found, in the online version, at doi:10.1016/j.snr.2024.100203.

References

[1] T.R. Naik, R.N. Kraus, R. Kumar, Influence of types of coarse aggregates on the coefficient of thermal expansion of concrete, J. Mater. Civ. Eng. 23 (2011) 467–472.
[2] R.B. Kogbara, S.R. Iyengar, Z.C. Grasley, E.A. Masad, D.G. Zollinger, A review of concrete properties at cryogenic temperatures: towards direct LNG containment, Constr. Build. Mater. 47 (2013) 760–770.
[3] C. Berwanger, A.F. Sarkar, Thermal expansion of concrete and reinforced concrete, Journal Proceedings (1976) 618–621.
[4] C.L. Page, Mechanism of corrosion protection in reinforced concrete marine structures, Nature 258 (1975) 514–515.
[5] A. Michel, M. Otieno, H. Stang, M.R. Geiker, Propagation of steel corrosion in concrete: experimental and numerical investigations, Cem. Concr. Compos. 70 (2016) 171–182.
[6] B.N. Popov, Corrosion engineering: Principles and Solved Problems, Elsevier, 2015.
[7] R. Mi, K.M. Liew, G. Pan, New Insights Into Diffusion and Reaction of CO2 Gas in Recycled Aggregate Concrete, 129, Cement and Concrete Composites, 2022 104486.
[8] Q. Shen, G. Pan, H. Zhan, Effect of interfacial transition zone on the carbonation of cement-based materials, J. Mater. Civ. Eng. 29 (2017) 04017020.
[9] D.W.S. Ho, R.K. Lewis, Carbonation of concrete and its prediction, Cem. Concr. Res. 17 (1987) 489–504.
[10] S. Zhang, L. Hou, H. Du, H. Wei, B. Liu, Y. Wei, A study on the interaction between chloride ions and CO2 towards carbon steel corrosion, Corros. Sci. 167 (2020) 108531.
[11] G.K. Glass, N.R. Buenfeld, Chloride-induced corrosion of steel in concrete, Prog. Struct. Mater. Eng. 2 (2000) 448–458.
[12] V. Gouda, Corrosion and corrosion inhibition of reinforcing steel: I. immersed in alkaline solutions, Br. Corros. J. 5 (1970) 198–203.
[13] D. Han, R.J. Jiang, Y.F. Cheng, Mechanism of electrochemical corrosion of carbon steel under deoxygenated water drop and sand deposit, Electrochim. Acta 114 (2013) 403–408.
[14] S.J. Jaffer, C.M. Hansson, Chloride-induced corrosion products of steel in cracked-concrete subjected to different loading conditions, Cem. Concr. Res. 39 (2009) 116–125.
[15] F.U.A. Shaikh, Effect of cracking on corrosion of steel in concrete, Int. J. Concr. Struct. Mater. 12 (2018) 3.
[16] M.B. Otieno, M.G. Alexander, H.-D. Beushausen, Corrosion in cracked and uncracked concrete – influence of crack width, concrete quality and crack reopening, Mag. Concr. Res. 62 (2010) 393–404.
[17] S. Imperatore, Z. Rinaldi, C. Drago, Degradation relationships for the mechanical properties of corroded steel rebars, Constr. Build. Mater. 148 (2017) 219–230.
[18] R. Songbo, G. Ying, K. Chao, G. Song, X. Shanhua, Y. Liqiong, Effects of the corrosion pitting parameters on the mechanical properties of corroded steel, Constr. Build. Mater. 272 (2021) 121941.
[19] D.J. Gohlke, J.C. Tanner, Gore-Tex® waterproof breathable laminates, J. Coat. Fabr. 6 (1976) 28–38.
[20] T. Kim, S. Jeon, S. Lone, S.J. Doh, D.-M. Shin, H.K. Kim, et al., Versatile nanodot-patterned Gore-Tex fabric for multiple energy harvesting in wearable and aerodynamic nanogenerators, Nano Energy 54 (2018) 209–217.
[21] Z.C. Grasley, D.A. Lange, M.D. D'Ambrosia, S. Villalobos-Chapa, Relative humidity in concrete, Concr. Int. 28 (2006) 51–57.
[22] J. Tao, Y. Luo, L. Wang, H. Cai, T. Sun, J. Song, et al., An ultrahigh-accuracy miniature dew point sensor based on an integrated photonics platform, Sci. Rep. 6 (2016) 29672.
[23] M. Azenha, J.L.D. Granja, Monitoring and simulating humidity profiles in concrete elements during drying, in: RILEM Proceedings, 2016.
[24] M. Monazami, A. Sharma, R. Gupta, Evaluating performance of carbon fiber-reinforced pavement with embedded sensors using destructive and non-destructive testing, Case Stud. Constr. Mat. 17 (2022) e01460.
[25] Y. Zhang, M. Zhao, J. Zhang, Q. Shao, J. Li, H. Li, et al., Excellent corrosion protection performance of epoxy composite coatings filled with silane functionalized silicon nitride, J. Polym. Res. 25 (2018) 130.
[26] H. Klemm, Silicon nitride for high-temperature applications, J. Am. Ceram. Soc. 93 (2010) 1501–1522.
[27] M. Arai, A. Kohno, Corrosion behavior of sintered silicon nitride ceramics in acid and alkaline solutions, Zairyo-to-Kankyo 44 (1995) 276–280.
[28] G. Hummer, J.C. Rasaiah, J.P. Noworyta, Water conduction through the hydrophobic channel of a carbon nanotube, Nature 414 (2001) 188–190.
[29] R. Evans, U.M.B. Marconi, P. Tarazona, Fluids in narrow pores: adsorption, capillary condensation, and critical points, J. Chem. Phys. 84 (1986) 2376–2399.
[30] J. Hughes, H. Armstrong, The dielectric constant of dry air, J. Appl. Phys. 23 (1952) 501–504.
[31] M. Uematsu, E. Frank, Static dielectric constant of water and steam, J. Phys. Chem. Ref. Data 9 (1980) 1291–1306.
[32] L. Palmer, A. Cunliffe, J. Hough, Dielectric constant of water films, Nature 170 (1952), 796–.
[33] Z. Huang, N. Geyer, P. Werner, J. De Boor, U. Gösele, Metal-assisted chemical etching of silicon: a review: in memory of Prof, Ulrich Gösele, Adv. Mater. 23 (2011) 285–308.
[34] X. Li, P. Bohn, Metal-assisted chemical etching in HF/H 2 O 2 produces porous silicon, Appl. Phys. Lett. 77 (2000) 2572–2574.
[35] A. Chourasia, D. Chopra, A Study of Si3N4 by XPS, Surf. Sci. Spectra 2 (1993) 117–122.
[36] P. Du, L. Liu, Y. Dong, W. Li, J. Li, Z. Liu, et al., Synthesis of hierarchically porous boron-doped carbon material with enhanced surface hydrophobicity and porosity for improved supercapacitor performance, Electrochim. Acta 370 (2021) 137801.
[37] E.W. Hansen, F. Courivaud, A. Karlsson, S. Kolboe, M. Stöcker, Effect of pore dimension and pore surface hydrophobicity on the diffusion of n-hexane confined in mesoporous MCM-41 probed by NMR—a preliminary investigation1Dedicated to Professor Lovat V.C. rees in recognition and appreciation of his lifelong devotion to zeolite science and his outstanding achievements in this field.1, Microporous Mesoporous Mater. 22 (1998) 309–320.
[38] H. Bi, K. Yin, X. Xie, J. Ji, S. Wan, L. Sun, et al., Ultrahigh humidity sensitivity of graphene oxide, Sci. Rep. 3 (2013) 2714.
[39] Z. Wang, L. Shi, F. Wu, S. Yuan, Y. Zhao, M. Zhang, The sol–gel template synthesis of porous TiO2 for a high performance humidity sensor, Nanotechnology 22 (2011) 275502.
[40] D.S. Vieira, P.R. Fernandes, H. Mukai, R.S. Zola, G.G. Lenzi, E.K. Lenzi, Surface roughness influence on CPE parameters in electrolytic cells, Int. J. Electrochem. Sci. 11 (2016) 7775–7784.

[41] H. Shao, J. Wang, W. He, J. Zhang, C. Cao, EIS analysis on the anodic dissolution kinetics of pure iron in a highly alkaline solution, Electrochem. Commun. 7 (2005) 1429–1433.

[42] V. Mišković-Stanković, I. Jevremović, I. Jung, K. Rhee, Electrochemical study of corrosion behavior of graphene coatings on copper and aluminum in a chloride solution, Carbon N Y 75 (2014) 335–344.

[43] F. Mansfeld, Tafel slopes and corrosion rates from polarization resistance measurements, Corrosion 29 (2013) 397–402.